ChemComm

ROYAL SOCIETY OF CHEMISTRY

COMMUNICATION

View Article Online
View Journal

Cite this: DOI: 10.1039/d5cc01649e

Received 24th March 2025,
Accepted 2nd July 2025

DOI: 10.1039/d5cc01649e

rsc.li/chemcomm

Structural advantage of keto-linked Fe-porphyrin polymer in boosting hydrogen evolution reaction†

Xiaoyu Zhai,[a] Kainan Wang,[a] Cheng Yuan,[a] Pengfei Chen,[a] Aijian Wang, *[a] Jun Qian, [a] Long Zhao, [a] Weihua Zhu *[a] and Danhong Shang[b]

Herein, we introduce Tp-FeTAPP synthesized from 2,4,6-triformylphloroglucinol (Tp) and iron-coordinated tetrakis(4-aminophenyl)porphyrin (FeTAPP), a non-precious metal catalyst for HER that surpasses existing HER catalysts. Its impressive HER performance, with a low overpotential of 140 mV, is attributed to optimized metal active sites, enhanced charge transfer, and efficient mass transport through its porous structure, ensuring both stability and sustainability.

Over the past decade, metalloporphyrins with highly conjugated π-electron systems have garnered considerable attention from both scientific and industrial communities.[1,2] Their low manufacturing cost, high availability, exceptional selectivity, and reactivity make them promising candidates to replace noble metal-based electrocatalysts for hydrogen evolution reaction (HER) applications in fuel cells and metal–air batteries.[3] However, challenges inherent to poor stability, mass transfer limitations, low density of catalytic active sites, and susceptibility to dissolution in electrolytes, have impeded their widespread applications.

To address these limitations, we present a novel strategy that integrates metalloporphyrin units into a robust porous organic polymer (POP) framework, thereby achieving enhanced structural stability, improved active site exposure, and superior charge transfer. POPs are highly attractive for electrocatalytic applications due to their designable porosity, large surface area, and adjustable functionalities.[4] Among them, keto-linked POPs are particularly appealing due to their excellent chemical stability and compatibility with harsh alkaline environments.[5]

Based on the discussion, we successfully synthesized three novel POP electrocatalysts, *i.e.* **Tp-MTAPP** (M = Fe, Ni, Fe–Ni), using a solvothermal method followed by coordination with different metal ions (Scheme 1). Comparative analysis revealed that the metal center plays a crucial role in determining the HER performance, and the optimized **Tp-FeTAPP** demonstrated exceptional activity and stability exceeding 27 h for the alkaline HER. Post-HER characterization confirmed the excellent structural integrity of the catalyst, distinguishing it from many unstable porphyrin analogues. This work introduces a versatile and modular platform for designing durable HER electrocatalysts by combining the advantages of metalloporphyrins and POPs.

To elucidate the formation of the POP and subsequent metalation process, FTIR spectroscopy was systematically conducted on the individual components. As illustrated in Fig. 1a, the reaction of starting monomers was unequivocally confirmed by the disappearance of characteristic peaks: specifically, the C=O stretching vibration of the aldehyde group at 1620 cm^{-1} and the broad N–H stretching vibration of TAPP in the range of 3100–3200 cm^{-1} in the **Tp-TAPP** spectrum. The emergence of a distinct vibration band at approximately 1590 cm^{-1}, corresponding to the C=N linkage in **Tp-TAPP**, provides strong evidence for the formation of imine bonds

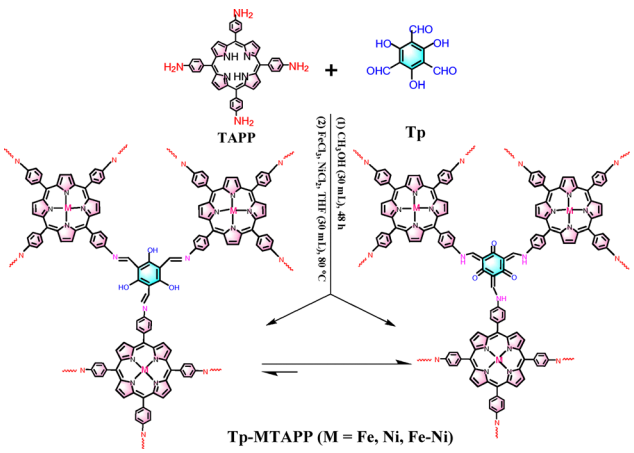

Scheme 1 Synthetic routes for **Tp-MTAPP** (M = Fe, Ni, Fe–Ni).

[a] School of Chemistry & Chemical Engineering, Jiangsu University, Zhenjiang 212013, P.R. China. E-mail: wajujs@ujs.edu.cn
[b] School of Environmental and Chemical Engineering, Jiangsu University of Science and Technology, Zhenjiang 212013, PR China

† Electronic supplementary information (ESI) available. See DOI: https://doi.org/10.1039/d5cc01649e

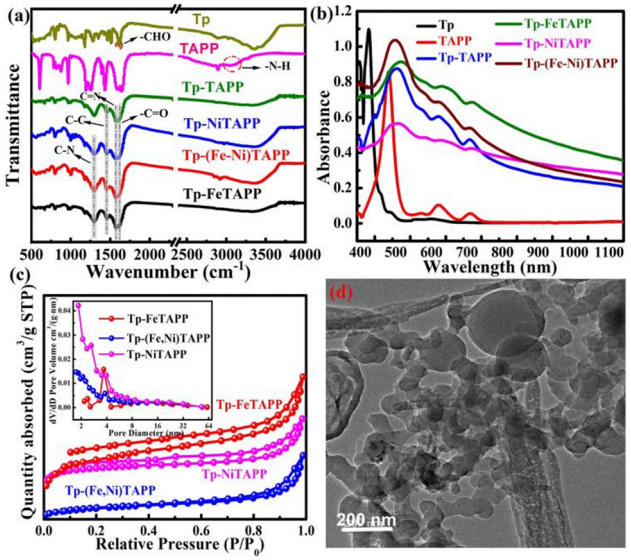

Fig. 1 (a) FTIR, (b) UV-vis absorption spectra, (c) N_2 adsorption–desorption isotherm analysis (inset is the corresponding pore size distribution) and (d) TEM image of **Tp-FeTAPP**.

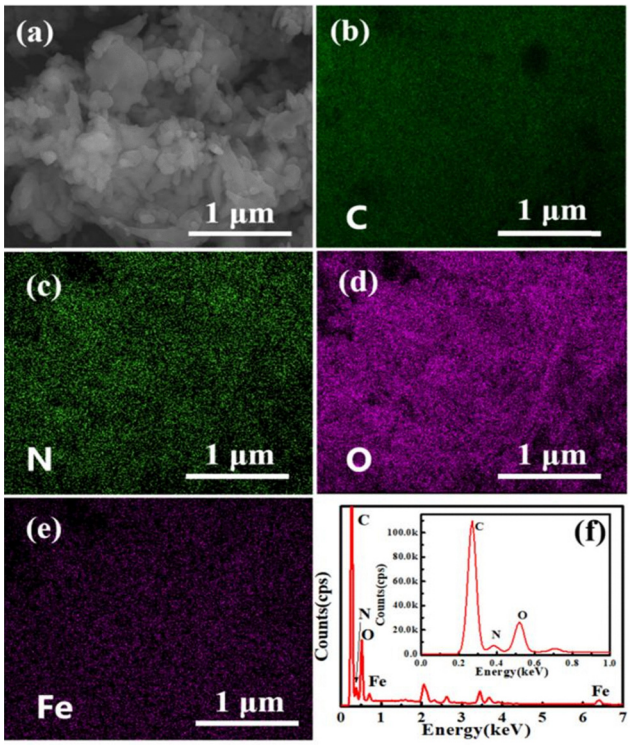

Fig. 2 SEM (a), elemental mapping images (b)–(e) and EDS image (f) of **Tp-FeTAPP**.

through the Schiff base reaction between the amino groups of TAPP and aldehyde units of **Tp**.[6] Furthermore, the **Tp-TAPP** spectrum revealed a characteristic peak at 1615 cm^{-1}, which can be attributed to the C═O stretching vibration, indicating the predominant existence of the keto tautomer over the enol form (Scheme 1).[6] For **Tp-NiTAPP**, peaks at 1001 and 1010 cm^{-1} (Ni–N vibrations) confirm Ni^{2+} coordination.[7] Similarly, **Tp-FeTAPP** and **Tp-(Fe–Ni)TAPP** show characteristic Fe–N and Ni–N bands, verifying successful metal incorporation and POP formation.

The UV-vis spectrum of **Tp-TAPP** (Fig. 1b) displays a broadened Soret band at 462 nm and reduced Q bands (500–750 nm), with a red-shift relative to TAPP due to extended π-conjugation.[8] Metal incorporation in **Tp-MTAPP** is evidenced by Soret band shifts and a reduction in Q band number. **Tp-FeTAPP** shows a 12–18 nm red-shift compared to **Tp-NiTAPP** and **Tp-(Fe–Ni)TAPP**, demonstrating enhanced electronic delocalization and confirming covalent linkage.[9] The nitrogen adsorption–desorption isotherm of **Tp-FeTAPP** (Fig. 1c) shows a mesoporous structure (3.2 nm, similar to other samples) and a high BET surface area of 228.5 $m^2\ g^{-1}$, higher than **Tp-NiTAPP** and much greater than **Tp-(Fe–Ni)TAPP**. The large surface area benefits HER by providing more active sites and improving mass transport.[10] The TEM image (Fig. 1d) reveals that **Tp-FeTAPP** consists of uniformly distributed nanoparticles with a quasi-spherical and tubular morphology. These nanoparticles appear to be aggregated into clusters. The porous nature of the assembly suggests potential for high surface area, favorable for electrocatalytic HER applications.

SEM analysis (Fig. 2a) reveals that **Tp-FeTAPP** possesses a compact, densely stacked morphology with layered features, indicating strong framework interactions. In contrast, **Tp-(Fe–Ni)TAPP** (Fig. S1a, ESI†) exhibits a looser, spherical-particle morphology, while **Tp-NiTAPP** (Fig. S1b, ESI†) shows a fibrous, network-like structure. These differences suggest that metal centers significantly influence the material assembly. The ordered and continuous structure of **Tp-FeTAPP** may offer advantages in stability and electronic connectivity, warranting further investigation. Additionally, elemental mapping analysis confirmed the successful doping of Fe and homogeneous distribution of all elements including C, N and O in the **Tp-FeTAPP** (Fig. 2b–e).[11,12] Quantitative EDS analysis determined the atomic composition of **Tp-FeTAPP** to be 75.36% carbon, 5.08% nitrogen, 18.18% oxygen, and 1.39% iron (Fig. 2f), which closely matches the expected elemental composition based on its theoretical structure.

The fine structure of the as-prepared materials was characterized using XPS. As depicted in Fig. 3a, all three materials (**Tp-NiTAPP**, **Tp-(Fe–Ni)TAPP**, and **Tp-FeTAPP**) contain their expected elemental compositions as designed. The high-resolution C 1s XPS spectrum of **Tp-FeTAPP** (Fig. 3b) exhibits five distinct peaks at approximately 284.1, 284.8, 285.6, 286.3, and 291.5 eV, which are attributed to C═C, C–C, C═N, C–N, and π–π* transitions, respectively.[13] Additionally, two peaks at 287.1 and 288.5 eV are assigned to the C–O and C═O functional groups, respectively. The high-resolution N 1s XPS spectrum of **Tp-FeTAPP** (Fig. 3c) is deconvoluted into three distinct bands at 399.3, 400.2, and 401.6 eV, corresponding to nitrogen species in C–N, Fe–N, and C═N linkages within **Tp-FeTAPP**, respectively.[14] The presence of an Fe–N peak provide strong evidence for the successful incorporation of Fe ions into the **Tp-FeTAPP** framework. In addition, another peak located at around 400.4 eV is attributed to the N–H bond in the keto tautomer of Tp-FeTPP. The presence of Fe^{2+} and Fe^{3+} was supported by XPS spectra (Fig. 3d). The presence of C–O and

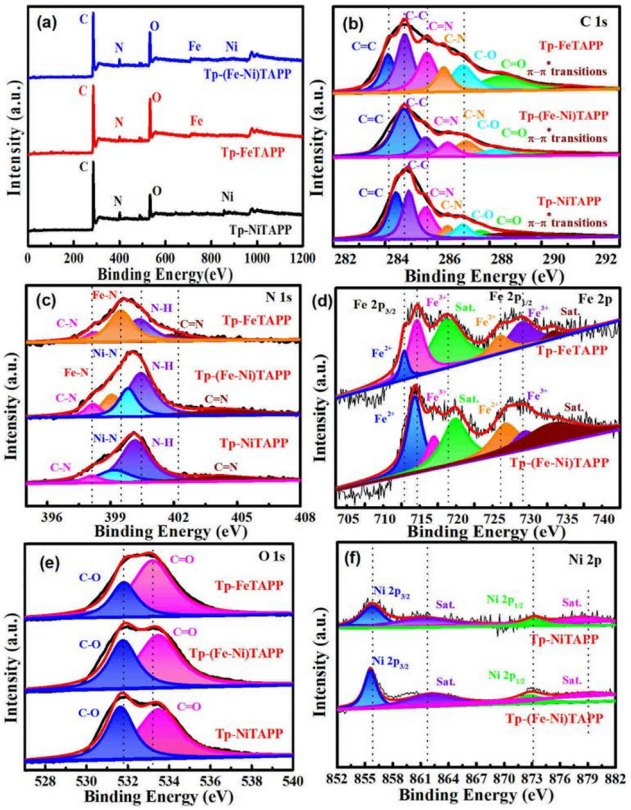

Fig. 3 (a) XPS survey spectra, and high-resolution XPS spectra of (b) C 1s, (c) N 1s, (d) Fe 2p, (e) O 1s and (f) Ni 2p.

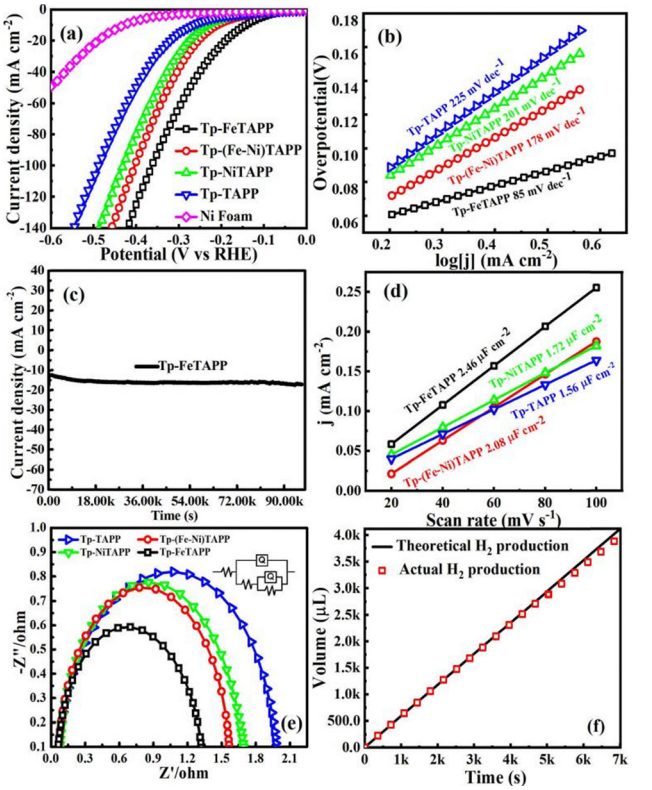

Fig. 4 (a) HER LSV polarization curves, (b) Tafel plots, (c) time-dependent HER stability in 1.0 M KOH solution, (d) apacitive current as a function of scan rates, (e) Nyquist plots and (f) the theoretical and detected volumes of generated hydrogen.

C═O species in **Tp-FeTAPP** (Fig. 3e) indicates the coexistence of the enol form and the keto tautomer, which aligns well with the results from the FTIR analysis. Comparative analysis reveals binding energy shifts in **Tp-FeTAPP** relative to both **Tp-NiTAPP** and **Tp-(Fe–Ni)TAPP** (Fig. 3b–e), suggesting modified electronic structures that may contribute to its enhanced HER activity. These compositional variations, combined with the Ni 2p chemical state differences (Fig. 3f), collectively influence their catalytic behaviors.

The HER performance of **Tp-FeTAPP** was evaluated in 1.0 M KOH using a three-electrode system. Polarization curves (Fig. 4a) show distinct activities among **Tp-FeTAPP**, **Tp-(Fe–Ni)TAPP**, and **Tp-NiTAPP**, with significant overpotential (η) differences at 10 mA cm^{-2}.[15] The NF substrate exhibited a high η value of 523 mV, consistent with its primary function as a conductive scaffold rather than an active catalyst. Strikingly, **Tp-FeTAPP** achieved an exceptionally low η of 140 mV, outperforming most previously reported non-precious metal-based HER catalysts (Table S1, ESI†). **Tp-FeTAPP** achieves a 39% overpotential reduction relative to **Tp-NiTAPP** and a 69 mV advantage over its bimetallic analogue. The different HER activity between **Tp-FeTAPP** and **Tp-(Fe–Ni)TAPP** further proves that only metal mixing cannot replicate the synergistic interplay of atomic-level Fe active sites and macroscale Ni-mediated conductivity.[16–18]

The HER reaction kinetics of the catalysts were investigated through Tafel slope analysis derived from the corresponding LSV curves. As illustrated in Fig. 4b, **Tp-FeTAPP** demonstrates superior HER kinetic performance with a low Tafel slope of 85 mV dec^{-1}, which is significantly lower than those of **Tp-(Fe–Ni)TAPP** (178 mV dec^{-1}), **Tp-NiTAPP** (201 mV dec^{-1}), and **Tp-TAPP** (225 mV dec^{-1}). This substantial reduction in the Tafel slope not only highlights the enhanced catalytic efficiency of **Tp-FeTAPP** but also suggests its favorable HER kinetics, as supported by previous studies.[19] The Tafel slope of **Tp-FeTAPP** falls within the characteristic range of 40–120 mV dec^{-1}, indicating that the HER process on its surface predominantly follows the Volmer–Heyrovsky mechanism.[20]

In addition, stability is a critical parameter in assessing the long-term catalytic performance of electrocatalysts for the HER.[21,22] Chronoamperometric measurements were performed in 1.0 M KOH. A timed-current response test revealed negligible variation in HER potential after 27.2 h of continuous operation (Fig. 4c). Post-HER characterization confirms the excellent structural stability of **Tp-FeTAPP**, as demonstrated by: (1) SEM/TEM showing preserved morphology with only slight aggregation (Fig. S2a and b, ESI†); (2) XRD patterns maintaining crystallinity except for additional Ni peaks from the substrate (Fig. S2c, ESI†); (3) unchanged XPS spectra verifying stable coordination environment (Fig. S2d, ESI†); and (4) identical Raman features indicating intact molecular structure (Fig. S2e, ESI†). These multi-technique analyses collectively evidence minimal dissolution or restructuring during HER operation.

The C_{dl} values, which are proportional to the ECSA,[23] were determined from CV measurements at various scan rates (Fig. 4d and Fig. S3, ESI†). Remarkably, **Tp-FeTAPP** exhibited a C_{dl} value of 2.46 μF cm^{-2}, higher than those of **Tp-(Fe–Ni)TAPP** (2.08 μF cm^{-2}), **Tp-NiTAPP** (1.72 μF cm^{-2}), and **Tp-TAPP** (1.56 μF cm^{-2}). This increases in C_{dl} directly correlates with a larger ECSA, which is importance for HER as it provides more exposed active sites for the HER process and facilitates the Volmer–Heyrovsky reaction kinetics. The Nyquist plots (Fig. 4e) show semicircles representing charge transfer resistance (R_{ct}), which reflects both HER kinetics and catalyst conductivity. **Tp-FeTAPP** displayed the lowest R_{ct} (11.32 Ω), indicating enhanced conductivity and faster electron transfer,[23–25] outperforming **Tp-(Fe–Ni)TAPP** (22.65 Ω), **Tp-NiTAPP** (45.87 Ω), and **Tp-TAPP** (65.76 Ω). These results align with the Tafel slopes, confirming its superior HER activity. **Tp-FeTAPP** exhibits a near-unity faradaic efficiency (~100%, Fig. 4f), confirming H_2 evolution as the dominant process with minimal side reactions, demonstrating exceptional HER selectivity.

The exceptional HER activity of **Tp-FeTAPP** originates from its well-defined Fe–N_4 coordination structure, which establishes critical structure–activity relationships. Electrochemical characterization reveals that the Fe–N_4 sites enable superior kinetics, as evidenced by a lower Tafel slope and reduced R_{ct} compared to Ni and bimetallic analogues.[26,27] The POP framework structure provides both high active site accessibility (confirmed by larger C_{dl} and BET surface area) and stability,[28] with XPS verifying preservation of the Fe^{2+}/Fe^{3+} redox states during operation.[26,28,29] These findings demonstrate how the single-metal Fe–N_4 configuration avoids the kinetic limitations of bimetallic systems while maintaining optimal site geometry for efficient HER.

In this study, three imide-bridged porphyrin POPs were synthesized for HER. **Tp-FeTAPP** showed optimal performance with 140 mV overpotential at 10 mA cm^{-2} (alkaline), surpassing both **Tp-NiTAPP**/**Tp-(Fe–Ni)TAPP** and prior reported systems (Table S1, ESI†). This enhancement stems from its favorable electronic structure, reduced R_{ct}, and larger ECSA, which collectively improve HER reaction kinetics. Our work provides a unique design approach for stabilizing metalloporphyrin catalysts through integration into a keto-linked POP framework. This strategy not only enhances catalytic performance but also offers long-term operational stability under alkaline HER conditions, representing a significant advancement over conventional porphyrin-based systems.

This research was funded by the National Natural Science Foundation of China (51506077), the College Students Innovation and Entrepreneurship Training Program (X2025102990489).

Conflicts of interest

There are no conflicts to declare.

Data availability

The data supporting this article have been included as part of the ESI.†

Notes and references

1 X. Li, H. Lei, L. Xie, N. Wang, W. Zhang and R. Cao, *Acc. Chem. Res.*, 2022, **55**, 878–892.
2 M. Liu, Y. Jiang, Z. Cao, L. Liu, H. Chen and S. Ye, *J. Energy Chem.*, 2024, **96**, 464–471.
3 Q. Ji, X. Yu, L. Chen, O. P. N. Yarley and C. Zhou, *Ind. Crops Prod.*, 2021, **172**, 114064.
4 T. Ashirov, J. Lim, A. Robles, T. Puangsamlee, P. W. Fritz, A. Crochet, X. Wang, C. Hewson, P. Iacomi, O. Š. Miljanić and A. Coskun, *Angew. Chem., Int. Ed.*, 2025, e202423809.
5 R. Liu, K. T. Tan, Y. Gong, Y. Chen, Z. Li, S. Xie, T. He, Z. Lu, H. Yang and D. Jiang, *Chem. Soc. Rev.*, 2021, **50**, 120–242.
6 B. C. Patra, S. Khilari, R. N. Manna, S. Mondal, D. Pradhan, A. Pradhan and A. Bhaumik, *ACS Catal.*, 2017, **7**, 6120–6127.
7 X. Li, C. Zhang, M. Luo, Q. Yao and Z.-H. Lu, *Inorg. Chem. Front.*, 2020, **7**, 1298–1306.
8 K. Zeng, Z. Tong, L. Ma, W.-H. Zhu, W. Wu and Y. Xie, *Energy Environ. Sci.*, 2020, **13**, 1617–1657.
9 W. Ji, T. X. Wang, X. Ding, S. Lei and B.-H. Han, *Coord. Chem. Rev.*, 2021, **439**, 213875.
10 Z. Li, Z. Tian, H. Cheng, T. Wang, W. Zhang, Y. Lu, Y. Lai and G. He, *Energy Storage Mater.*, 2023, **59**, 102764.
11 S. Qiao, B. Zhang, Q. Li, Z. Li, W. Wang, J. Zhao, X. Zhang and Y. Hu, *ChemSusChem*, 2019, **12**, 5032–5040.
12 S. Liu, Z. Zhang, K. Dastafkan, Y. Shen, C. Zhao and M. Wang, *Nat. Commun.*, 2025, **16**, 773.
13 X. Zhang, Y. Zhou, X. Huang, X. Hu, X. Huang, L. Yin, Q. Huang, Y. Wen, B. Li, J. Shi and X. Zou, *Food Chem.*, 2023, **407**, 135115.
14 J. Guo, L. Wang and J. Huang, *Ind. Eng. Chem. Res.*, 2020, **59**, 3205–3212.
15 J. Liang, H. Li, L. Chen, M. Ren, O. A. Fakayode, J. Han and C. Zhou, *Ind. Crop. Prod.*, 2023, **193**, 116214.
16 H. Hu, Y. Zheng, Y. Zhu, L. Qian, Z. Yuan, Y. Dai, T. Zhang, D. Yang and F. Qiu, *Inorg. Chem.*, 2023, **62**, 20250–20257.
17 Y. Wang, D. Chao, Z. Wang, J. Ni and L. Li, *ACS Nano*, 2021, **15**, 5420–5427.
18 M. Liu, C. Zhang, A. Han, L. Wang, Y. Sun, C. Zhu, R. Li and S. Ye, *Nano Res.*, 2022, **15**, 6862–6887.
19 F. Sun, Q. Tang and D. Jiang, *ACS Catal.*, 2022, **12**, 8404–8433.
20 L. Qian, H. Hu, Y. Zheng, Y. Zhu, Z. Yuan, Y. Dai, T. Zhang, D. Yang and F. Qiu, *Inorg. Chem.*, 2024, **63**, 1682–1691.
21 L. Wang, C. Zhang, Z. Cao, G. Zeng, J. Liu and S. Ye, *Adv. Funct. Mater.*, 2024, **34**, 2406670.
22 H. Cao, X. Wen, X. Luo, L. Ma, Z. Xu, Z. Zhang and W. Zhang, *Angew. Chem., Int. Ed.*, 2024, **63**, e202411683.
23 H. Hu, Y. Zheng, Y. Zhu, L. Qian, Z. Yuan, Y. Dai, T. Zhang, D. Yang and F. Qiu, *Colloids Surf., A*, 2023, **679**, 132572.
24 Z. Bin, L. Feng and Y. Yan, *Food Chem.*, 2022, **388**, 132898.
25 E. Han, L. Li, T. Gao, Y. Pan and J. Cai, *Food Chem.*, 2024, **437**, 137773.
26 Y. Sasaki, A. Iwase, H. Kato and A. Kudo, *J. Catal.*, 2008, **259**, 133–137.
27 M. Liu, J. Zhu, Y. Liu, F. Gong, R. Li, H. Chen, M. Zhao, Q. Jiang, J. Liu and S. Ye, *Chem. Eng. J.*, 2022, **446**, 137080.
28 D. Wang, X. Wang, Y. Lu, C. Song, J. Pan, C. Li, M. Sui, W. Zhao and F. Huang, *J. Mater. Chem. A*, 2017, **5**, 22618–22624.
29 X. Wang, Y. Pan, X. Wang, Y. Guo, C. Ni, J. Wu and C. Hao, *Ind. Crop. Prod.*, 2022, **189**, 115863.

